Assessment of Ultrasonic Phased Array Inspection Method for Welds in Cast Austenitic Stainless Steel Pressurizer Surge Line Piping

Carol A. Nove*, Wallace E. Norris*, Aaron A. Diaz, Michael T. Anderson****
*U.S. Nuclear Regulatory Commission
Washington, DC 20555, 301-415-7000
** Pacific Northwest National Laboratory
Richland, Washington 99352, 1-888-375-7665

BACKGROUND

Research is being conducted for the U.S. Nuclear Regulatory Commission (NRC) at the Pacific Northwest National Laboratory to assess the effectiveness and reliability of advanced nondestructive examination (NDE) methods for the inspection of light water reactor (LWR) components. The scope of this research encompasses primary system pressure boundary materials including cast austenitic stainless steels (CASS), dissimilar metal welds (DMWs), piping with corrosion-resistant cladding (CRC), weld overlays, inlays and onlays, and far-side examinations of austenitic piping welds. A primary objective of this work is to evaluate various NDE methods to assess their ability to detect, localize, and size cracks in coarse-grained steel components. In early FY-2007, the NRC published NUREG/CR-6933, *Assessment of Crack Detection in Heavy-Walled Cast Stainless Steel Piping Welds Using Advanced Low-Frequency Ultrasonic Methods*[1], which provided a detailed description of the inspection challenges posed by CASS as it relates to the microstructures and component geometries of primary piping loop configurations with thicknesses of approximately 76.2 mm (3-in.). However, thinner cast piping welds exist in pressurized water reactors (PWRs), such as on pressurizer (PZR) surge lines and safe-ends to DMWs, and optimum frequencies and ultrasonic phased-array (PA) inspection parameters have yet to be established to examine relatively thin CASS components. A decision was made to initiate work on these smaller diameter, thinner pipes in response to cracking associated with pressurizers. For example, on December 11, 2006, the NRC published Information Notice 2006-27, "Circumferential Cracking in the Stainless Steel Pressurizer Heater Sleeves of Pressurized Water Reactors," to describe an occurrence in which a licensee attributed a circumferentially-oriented crack to intergranular stress corrosion cracking (IGSCC) in a stainless steel pressurizer heater sleeve in a pressurized water reactor (PWR) coolant environment. This particular event challenged the previously held belief that stainless steel PZR heater sleeves in PWRs were not susceptible to IGSCC. This paper summarizes the capabilities of PA ultrasonic testing (UT) methods as applied to the inspection of welds in CASS PZR surge line nuclear reactor piping.

A set of thermal fatigue cracks (TFCs) were implanted into three CASS PZR surge-line specimens (pipe-to-elbow welds) that were fabricated using vintage CASS materials formed in the 1970s, and flaw responses from these cracks were used to evaluate detection and sizing performance of the PA-UT methods applied. This effort was comprised of multiple elements that included use of microstructural knowledge (dimensional analysis, grain orientation, and grain type) as well as sound field modeling to more effectively modify inspection parameters and enhance the inspection outcomes. Advanced probe design and sound field simulations were employed to enhance detection and characterization of circumferentially oriented flaws, and an assessment of lateral (circumferential) flaw localization capability and performance was also conducted. An evaluation of flaw detection, length sizing, depth sizing, and signal-to-noise ratio (SNR) was performed for all flaws in the subject specimens, as a function of various inspection parameters, and finally, measurements were made to quantify and assess the baseline CASS material noise and its potential impact on flaw detection.

SPECIMENS

Previous work has been focused on heavy-walled primary loop piping components with outer diameters (OD) ranging from 71.12 to 91.44 cm (28 to 36 in.). However, a variety of thinner cast piping welds, with OD measurements ranging from approximately 20.48 to 35.56 cm (12 to 14 in.) exist in PWRs, specifically in PZR surge lines and safe ends used in Combustion Engineering (CE) designed plants. These smaller bore piping networks typically exhibit wall thicknesses ranging from 3.05 to 4.32 cm (1.2 to 1.7 in.), which is approximately half that of the larger bore, primary loop piping components. These specimens were fabricated from piping

components salvaged from CE-designed units that were never brought to full operation. The material comprising these components include both centrifugally cast stainless steel (CCSS) pipe segments and statically cast stainless steel (SCSS) elbows, with dimensions of approximately 30.5- to 35.5-cm (12- to 14-in.) outside diameter (OD) and approximately 33-mm (1.3-in.) wall thickness (Figure 1).

The CASS PZR surge-line specimens used in this study were sliced, polished, and chemically etched to highlight the microstructures of both pipe and elbow segments. Microstructural analyses were conducted, and dimensional results provided insights into the inspection wavelength-to-grain diameter ratios. Grain diameters ranged from very small 0.5 mm (0.02 in.) to very large 41.0 mm (1.61 in.). Table 1 shows the average grain size and range from each of the surge-line specimens.

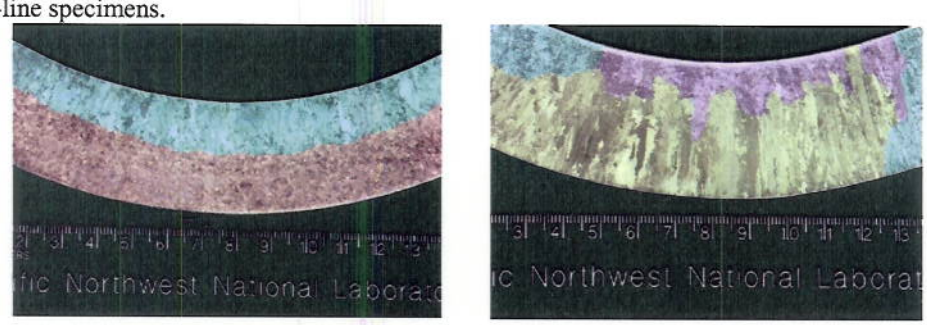

Figure 1: Photographs of polished and chemically etched CASS PZR Ring Segment showing the pipe-side (CCSS) grain microstructure (left) and the elbow-side (SCSS) grain microstructure (right). (Note that false colors have been added to assist the viewer in judging microstructural transitions, variation and banding.)

Table 1: Grain diameter measurements from the three PZR surge-line specimens

	Surge Line 1 Grain Diameter (7C-059), mm (in.)		WNP3 Surge Line Grain Diameter (9C-001 and 9C-002), mm (in.)		
	Elbow	**Pipe**	**Elbow**	**Pipe Center**	**Pipe Outside**
Average	2.6 (0.10)	1.9 (0.07)	10.3 (0.41)	6.6 (0.26)	3.5 (0.14)
Minimum	0.5 (0.02)	0.6 (0.02)	2.6 (0.10)	1.3 (0.05)	0.8 (0.03)
Maximum	6.3 (0.25)	6.7 (0.26)	41.0 (1.61)	25.6 (1.01)	13.9 (0.55)

The first CASS PZR specimen that was fabricated (7C-059) was comprised of moderately sized grains where the microstructure was believed to be less attenuative and thereby slightly less challenging to the PA inspection methods applied in the study. The four thermal fatigue cracks implanted in this specimen were deeper (ranging from 30% through-wall to 50% through-wall) in order to obtain some initial baseline PA data. Results from this initial assessment were very positive; therefore, shallower cracks were implanted in the two 9C specimens (ranging from 10% through-wall to 30% through-wall). This provided a more diverse set of flaws (depth-wise) in specimens with more challenging microstructures, effectively allowing the study to push the detection limits as well as the sizing limits for the PA approach. All of the flaws were implanted within the weld metal (with the exception of flaw 2 in specimen 7C-059) to minimize the potential for disturbing the parent material or introducing implantation anomalies that might result in reflection of coherent sound energy. Table 2 provides a summary of all of the implanted thermal fatigue flaws.

PHASED ARRAY ULTRASONIC EXAMINATIONS

PA-UT examinations were performed on implanted/fabricated TFCs to evaluate detection, localization, and sizing performance as a function of frequency. Four different custom-designed PA probes were employed in this study, operating nominally at 800 kHz, 1.0 MHz, 1.5 MHz, and 2.0 MHz center frequencies. Data were acquired as a function of inspection frequency, inspection angle (30° to 70° in 1° increments), and from both the CCSS pipe side and from the SCSS elbow side of the weld.

Examples of the merged data file analysis setup for flaw 1 on specimen 9C-002 is provided in Figures 2 and 3 for frequencies of 800 kHz and 2.0 MHz, respectively. Merged files are essentially composite images that use signal response information from all angles. Merged data were used for length sizing and SNR analyses. These images depict the composite (merged data from all angles) Sector-scan side view in the upper left portion of the analysis

Table 2: Summary table depicting true-state dimensions and locations of all thermal fatigue flaws in all three CASS PZR surge-line specimens. Note that all flaws are oriented in the circumferential direction.

Flaw	Flaw Location	Flaw Length, cm (in.)	Flaw Depth (Height) in % of thickness	Degree Location
1-1	Weld Centerline	10.2 (4.0)	35.2% T	45°
1-2	Pipe Side Near Fusion Line	5.1 (2.0)	30.3% T	120°
1-3	Weld Centerline	5.1 (2.0)	29.8% T	210°
1-4	Weld Centerline	15.2 (6.0)	30.4/50.2% T	300°
2-1	Weld Centerline	7.6 (3.0)	10/20% T	0°
2-2	Weld Centerline	5.1 (2.0)	28.6% T	90°
2-3	Weld Centerline	6.4–7.6 (2.5–3.0)	27.1% T	270°
3-1	Weld Centerline	7.6 (3.0)	16/25.1% T	0°
3-2	Weld Centerline	5.1 (2.0)	20.6% T	90°
3-3	Weld Centerline	6.4–7.6 (2.5-3.0)	16% T	270°

window. The composite C-scan (top-view) images are provided in the upper right portion of the analysis window. The composite D-scan (end-view) images are shown in the lower right portion of the analysis window. And finally, a sectioned polar view is provided in the lower left portion of the analysis window, showing the circumferential aspect of the flaw responses as a function of through-wall depth. On the images in Figures 2, the corner trap signal from the ID surface-connected crack is clearly evident in the Sector-, C- and D-scan views. Image analysis employed various views of the detected flaws for both length and depth sizing. The depth-contour of the flaw is seen in the D-scan end view and to a lesser degree in the polar view provided on the left side of Figure 2. This portion of the flaw signal accurately represents the transition of the depth of the flaw from one depth (approximately 15% through-wall) to the deeper portion of the flaw (approximately 25% through-wall). A red arrow indicates this feature in the lower-right portion of the analysis window shown in the right side of Figure 2. Figure 3 shows data collected on flaw 1 of 9C-002 at 2.0 MHz. Though the corner trap signal responses from the ID surface-connected crack are evident in each of the views, the signal response continuity and strength has begun to decrease. This is

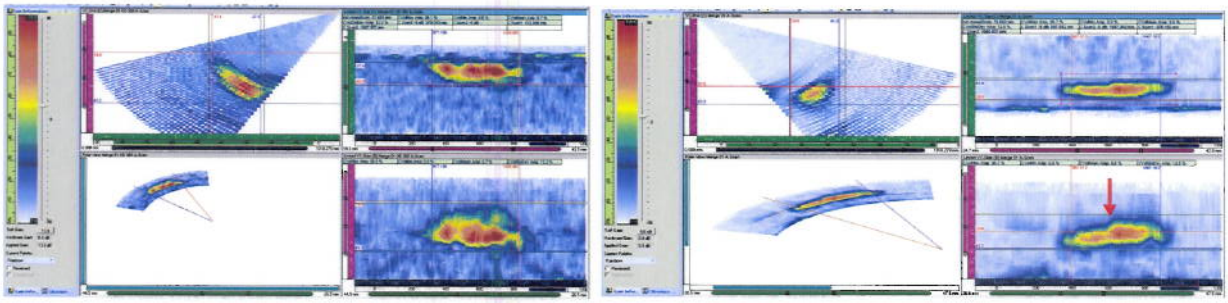

Figure 2: 800-kHz data showing flaw 1 from pipe side of 9C-002 (left) and elbow side of 9C-002 (right), merged image for length sizing.

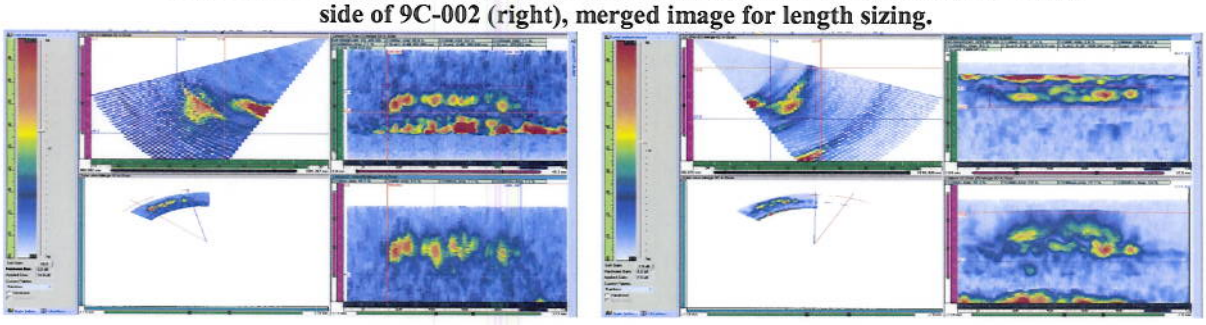

Figure 3: 2.0 MHz data showing flaw 1 from pipe side of 9C-002 (left) and elbow side of 9C-002 (right), merged image for length sizing.

expected as the effects of the anisotropic and inhomogeneous microstructures begin to have a more adverse effect on sound field propagation with increased inspection frequency. A comparative analysis of the pipe-side and elbow-side images in these two figures visually shows the differences in background clutter between the CCSS and SCSS parent material and indicates that even at a relatively higher frequency, the PA results show that an effective inspection can be conducted, and relatively accurate sizing data can be computed, in these coarse-grained materials.

As part of the data analyses, the flaw lengths and depths were sized and signal-to-noise determinations were made. Flaw lengths were measured at the half amplitude (−6 dB) points on the flaw corner signals. The results for all inspection frequencies and all specimens are listed in Tables 3 and 4 summarizing length measurements and depth measurements relative to the true-state data for the flaws. Where tip signals are not detected, the depths of the

Table 3: Length sizing summary of results

		800 kHz		1.0 MHz		1.5 MHz			2.0 MHz	
Specimen/ Flaw	True-State Length, mm	CCSS, mm	SCSS, mm	CCSS, mm	SCSS, mm	CCSS, mm	Raster CCSS, mm	SCSS, mm	CCSS, mm	SCSS, mm
7C-059										
1	101.6	104.7	114.9	116.1	112.9	116.5		102.4	119.3	96.6
2	50.6	63.0	19.1	69.2	61.4	34.8		34.8	36.0	57.1
3	50.6	72.0	--	49.3	39.3	49.7		74.0	45.8	62.4
4	152.6	190.5	160.2	186.4	181.2	187.3		181.3	181.4	143.3
9C-001										
1	76.6	89.3	92.3	96.3	94.5	91.5	76.6	83.3	104.4	77.4
2	51.1	56.4	74.5	59.2	72.8	64.1	51.1	46.8	37.8	57.8
3	69.7	77.1	69.4	70.3	77.1	88.4	69.7	69.1	93.2	64.0
9C-002										
1	76.7	68.6	79.9	100.3	96.5	62.0	88.2	79.0	101.3	90.5
2	50.5	53.2	67.2	57.4	73.9	53.3	50.3	63.3	54.1	66.9
3	69.7	60.8	70.2	68.0	91.0	55.3	54	55.3	53.8	71.9
RMSE		***15.7***	***16.0***	***16.6***	***18.5***	***16.9***	***8.0***	***14.4***	***19.4***	***9.1***

Table 4: Depth sizing summary of results

		800 kHz		1.0 MHz		1.5 MHz			2.0 MHz	
Specimen/ Flaw	True State Length, mm	CCSS, mm	SCSS, mm	CCSS, mm	SCSS, mm	CCSS, mm	Raster CCSS, mm	SCSS, mm	CCSS, mm	SCSS, mm
7C-059										
1	10.9	12.6	11.5	10.6	11.8	10.9		11.5	11.4	10.6
2	9.3	11.6	9.6	11.3	9.1	9.2		8.3	10.9	10.5
3	9.3	9.8	--	10.4	10.0	10.6		10.0	11.1	10.3
4	15.6	16.3	14.5	15.0	14.7	14.5		14.9	15.0	15.3
9C-001										
1a	3.4	5.0	4.0	3.4	3.2	4.2	3.5	2.5	3.5	5.2
1b	6.4	7.5	7.9	5.8	6.2	5.7	5.2	7.7	6.1	6.9
2	8.9	8.6	8.0	7.7	7.1	8.1	7.1	9.2	11.5	11.2
3	8.3	11.1	7.2	9.7	9.0	8.8	7.8	7.7	10.3	9.0
9C-002										
1a	4.8	4.3	6.9	4.8	NA	4.3	4.2	4.5	4.4	5.8
1b	7.5	9.5	7.9	9.3	6.4	7.4	6.5	4.6	7.9	9.0
2	6.3	6.4	8.1	7.9	8.2	6.6	6.7	4.4	6.0	7.0
3	4.8	6.3	NA	6.5	3.6	5.3	8.3	5.1	6.0	6.9
RMSE		***1.5***	***1.8***	***1.2***	***1.7***	***0.7***	***1.5***	***1.2***	***1.3***	***1.3***

flaws are based on specular reflections from the upper portions of the flaws; therefore, the full extent of the crack depths may not be accurately measured. However, the results are still quite good and tend to oversize the crack depths, suggesting that indeed the top of the cracks were detected. Root mean square error (RMSE) calculations for the 10 flaws as inspected from either the CCSS pipe side or the SCSS elbow side of the surge lines, as a function of inspection frequency, are also shown.

SNRs were calculated for the corner signals of the flaw responses from both the CCSS (pipe) and SCSS (elbow) sides. The SNR was determined from the peak signal response and an average noise value at the same part path. Summary SNR results for all inspection frequencies and specimens are listed in Table 5. The lowest SNR for the 800-kHz probe across all flaws in these specimens was 10.4 dB, while the highest SNR for the 800-kHz data was 24.6 dB, indicating minimal sound field attenuation effects due to the microstructure.

The detection and sizing data showed that all the implanted TFCs in all three specimens were detected from both the centrifugally cast stainless steel (CCSS pipe) and the statically cast stainless steel (SCSS elbow) sides of the weld at all inspection frequencies. Data at 800 kHz were not collected on one of the cracks from the SCSS elbow side due to geometrical constraints that precluded effective coupling of the PA probe. The results reported here show that longitudinal mode, transmit-receive matrix phased-array probes over a wide frequency range, can provide effective sound fields for detection and characterization of TFCs in CASS PZR surge line components. PA-UT results were compared against true-state data for all flaws, and root mean square error (RMSE) was computed as a metric for both length sizing and depth sizing of the flaws in this study. Also, SNR measurements were made and SNR values were computed and documented for all flaws and scanning scenarios.

Table 5: Signal-to-Noise Ratio Summary of Results

	800 kHz		1.0 MHz		1.5 MHz			2.0 MHz	
Specimen/ Flaw	**CCSS, dB**	**SCSS, dB**	**CCSS, dB**	**SCSS, dB**	**CCSS, dB**	**Raster CCSS, dB**	**SCSS, dB**	**CCSS, dB**	**SCSS, dB**
7C-059									
1	17.0	15.7	16.6	18.3	14.7		18.7	18.2	22.4
2	13.7	10.4	14.2	11.4	14.3		11.6	16.9	11.1
3	14.5	--	16.2	9.5	17.7		17.5	19.9	18.1
4	15.1	17.4	16.3	15.8	17.3		16.6	15.7	19.0
9C-001									
1	20.0	15.2	20.7	14.2	21.1	22.6	16.3	19.4	18.1
2	19.6	15.5	18.9	14.0	17.8	21.3	15.1	20.7	15.6
3	17.4	13.7	17.2	18.1	16.4	17.4	18.9	15.5	16.7
9C-002									
1	16.6	24.6	16.8	22.6	17.6	18.4	11.2	18.3	16.5
2	13.9	20.0	14.9	21.0	15.9	19.7	21.7	17.5	19.9
3	17.2	16.7	18.0	19.7	18.1	18.9	17.3	17.1	17.9

A key benchmark used for determination of the effectiveness and utility of the inspection approach is to compare the composite length sizing and depth sizing results from the evaluation against the American Society of Mechanical Engineers (ASME) Boiler and Pressure Vessel Code (Code), Section XI acceptance criteria for both length and depth sizing. The length sizing criterion calls for an RMSE less than 19.05 mm (0.75 in.), while the depth sizing criterion calls for an RMSE less than 3.81 mm (0.125 in.). Length sizing measurements (individual data files) were split among three different analysts, each taking specific portions of data to size. A majority of the data was straight forward and easily sized at the −6 dB level, but some data required interpretation due primarily to a noncontiguous signal. This interpretation is likely to add a human factors error into the data, either elongating or shortening the length values.

Regarding detection capability, all of the flaws were detected with the exception of flaw 3 in specimen 7C-059 as seen from the SCSS elbow at 800 kHz. As noted earlier, data could not be collected on this flaw because of the large footprint of the probe and the elbow geometry on the intrados. Signal-to-noise values were very good showing that flaw detection was not an issue. The data show that flaws are detectable at frequencies up to 2.0 MHz in these surge-line specimens containing grain sizes as large as 41 mm (1.61 in.) and nominal wall thickness of 33 mm (1.30 in.). The length sizing performance is slightly degraded by using a 2.0-MHz inspection as observed from the

CCSS side of the weld. From this data set, the length sizing RMSE falls outside of the ASME Code-allowable limit at 2 MHz. Length sizing error was larger on specimen 7C-059 than on the two 9C specimens. This is in part due to surface irregularities relative to the probe footprints, differences in surface finish (both of which impact coupling efficiency), and the unanticipated detection of artifacts and/or anomalies associated with the crack implantation process. While all of the flaws were specified to be implanted within the weld metal (with the exception of flaw 2 in specimen 7C-059) to minimize the potential for disturbing the parent material or introducing implantation anomalies that might result in reflection of coherent sound energy, the data appear to indicate that these effects still exist and are detectable. A review of radiographs provided by the flaw manufacturer indicated the existence of flaw implantation artifacts that were also detected with the PA ultrasonic method evaluated here. The length sizing performance is improved in the raster data as compared to the line scan data as observed in a comparison of the CCSS data at 1.5 MHz. Raster scanning more fully captures the flaw response signals because it acquires data over many axial locations. Line scan data is acquired from one axial position which may not be the optimum location. A review of Table 4 shows that flaw depth sizing was completely within the ASME Code-allowable limit, even at 2 MHz.

The reported SNR values provided in Table 5 were calculated from the peak signal responses and the mean noise responses obtained at the same part path in dB. These calculated values are all very good, indicating minimal attenuation effects on sound field propagation over the frequency range from 800 kHz to 2.0 MHz. Flaw detection was not in question for the TFCs implanted in these specimens as shown by the high SNRs. For the materials used in this study, adequate SNRs were achieved even at 2.0 MHz and raster data SNRs are similar to the line scan data SNRs. If CASS piping with greater attenuative properties is encountered in the field, the use of lower frequencies (800 kHz to 1.0 MHz) would be more appropriate for inspection. The elbow configuration limited elbow-side access to flaw 3 in specimen 7C-059, but all other flaws were detected from both the pipe and elbow sides of the welds. The lowest SNR value for all signal responses in this study was computed to be 9.5 dB while the maximum SNR value was 24.6 dB.

The issue of sound beam redirection and the potential for circumferential error in the positional registration of flaw responses relative to the true position of the probe on the part surface was also addressed. The measured localization data were compared to the true-state flaw position data on the specimens, and this information was plotted and analyzed to determine if beam redirection and localization of the cracks were significantly affected by the microstructures. Figures 4 through 6 map the flaw length positional data with true state, for each of the specimens. The measurements were based on a −6 dB drop method with some analyst interpretation involved to account for signal dropout or other anomalies in the signals. The pipe- and elbow-side data are separated as well as probe frequency. This mapping allows one to identify trends in over- or under-sizing of the flaws and for redirection of the sound beam, which can be observed in cast material.

For specimen 7C-059, the 0° reference point lies at the far left of the plot at 0 mm. For the 9C specimens, a flaw was centered at the 0° reference point so the horizontal axis was shifted to start at −150 mm. The horizontal line (X-axis) on the plots represents linear distance (corresponding to the circumferential position of the flaws) around the circumference of the pipe specimens in millimeters. Lines that are plotted above the X-axis are measured flaw lengths from each of the four PA probes acquired from data taken from the CCSS pipe side of the specimens. Lines that are plotted below the X-axis are measured flaw lengths from each of the four PA probes as obtained from the SCSS elbow side of the specimens. Lines that lie directly on the X-axis horizontal line represent the true-state

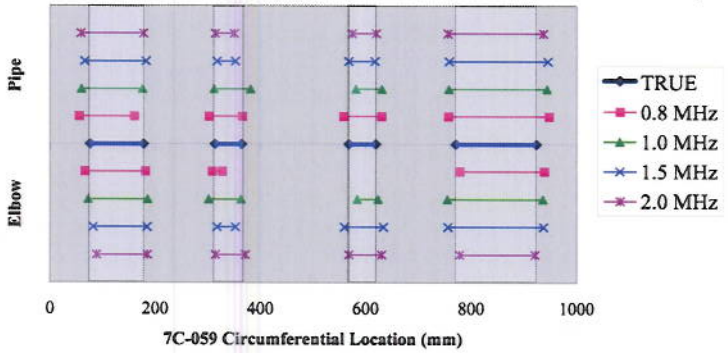

Figure 4: Map of true-state and measured, circumferential flaw localization data for specimen 7C-059.

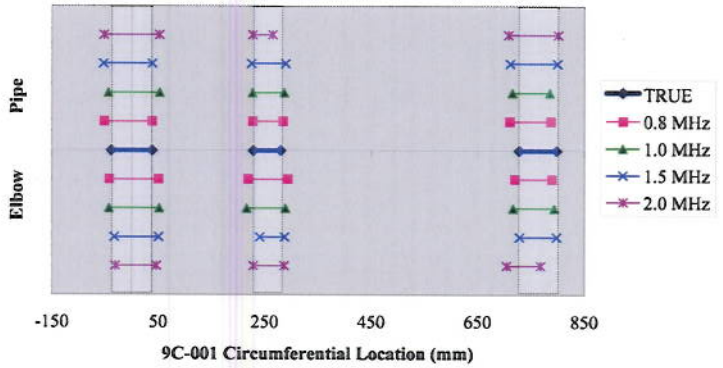

Figure 5: Map of true-state and measured, circumferential flaw localization data for specimen 9C-001.

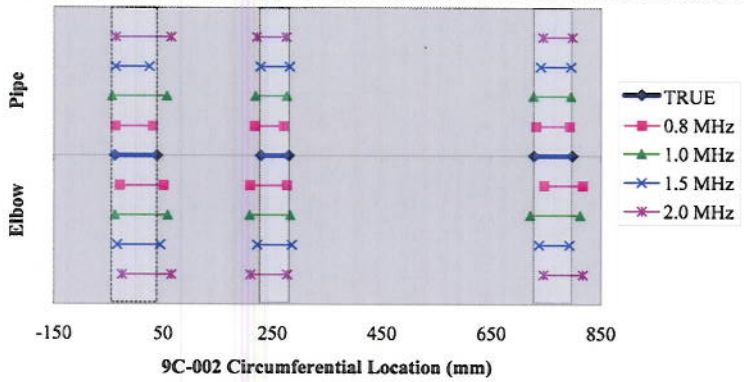

Figure 6: Map of true-state and measured, circumferential flaw localization data for specimen 9C-002.

lengths and circumferential positions of the flaws in the specimen. The true-state data regions are additionally marked as lighter shaded regions in the plots for improved contrast and easier data comparisons. Flaws are plotted in ascending order from left to right on each of the plots. Therefore, on specimen 9C-002 for example, flaw 1 is centered at the 0-mm mark, flaw 2 is centered at the 250-mm mark, and flaw 3 is centered at the 750-mm mark. In general, flaw 4 at an 850-mm circumferential position in specimen 7C-059; flaw 1 at a 0-mm circumferential position and flaw 2 at 250-mm circumferential in specimen 9C-001; and flaw 1 at a 0-mm circumferential position in specimen 9C-002 tend to be oversized. Flaw 2 at a 340-mm circumferential position in specimen 7C-059 tends to be undersized. The remaining flaws were both over and undersized.

A trend toward over sizing of the flaw lengths can be expected as the probe spot size will inherently be added to the ultrasonic measurement values. Additional error could come from the flaw implantation technique itself because the specimen is excavated and the flaw coupon implanted via weld material. Ultrasound may be sensitive to the excavation boundary and/or the added weld material. Lateral beam redirection does not seem to be a significant issue in these data. There does not appear to be a left or right bias in start or end positions of the mapped flaws.

CONCLUSION

In conclusion, state-of-the-art phased-array inspection approaches are rapidly evolving and the capability to reliably detect and effectively characterize 10%–50% through-wall TFCs in CASS components where the wall thickness is generally less than 50 mm (2.0 in.) has been demonstrated here. PA-UT data obtained using inspection frequencies ranging from 800 kHz to 2.0 MHz yielded strong SNRs and provided accurate length and depth sizing results. While additional questions remain to be answered, long-wavelength ultrasonic approaches coupled with advanced signal processing technologies are beginning to show signs of success toward addressing this challenging inspection issue.

REFERENCES

1. Anderson MT, Crawford SL, Cumblidge SE, Denslow KM, Diaz AA and Doctor SR, *Assessment of Crack Detection in Heavy-Walled Cast Stainless Steel Piping Welds Using Advanced Low-Frequency Ultrasonic Methods.* NUREG/CR-6933, PNNL-16292, U.S. Nuclear Regulatory Commission, Washington, D.C., 2007.